Bioorganic Chemistry xxx (xxxx) xxxx

Contents lists available at ScienceDirect

Bioorganic Chemistry

journal homepage: www.elsevier.com/locate/bioorg

Discovery of 5-aryl-3-thiophen-2-yl-1H-pyrazoles as a new class of Hsp90 inhibitors in hepatocellular carcinoma

Samy Mohamady[a,*], Muhammad I. Ismail[a], Samar M. Mogheith[b], Yasmeen M. Attia[c,*], Scott D. Taylor[d]

[a] Department of Pharmaceutical Chemistry, Faculty of Pharmacy, The British University in Egypt, Al-Sherouk City, Cairo-Suez Desert Road, 11837 Cairo, Egypt
[b] Faculty of Pharmacy, The British University in Egypt, Egypt
[c] Department of Pharmacology, Faculty of Pharmacy, The British University in Egypt, Al-Sherouk City, Cairo-Suez Desert Road, 11837 Cairo, Egypt
[d] Department of Chemistry, University of Waterloo, 200 University Avenue West, Waterloo, Ontario N2L 3G, Canada

ARTICLE INFO

Keywords:
Diarylpyrazole
Heat shock proteins
Hsp90
Pyrazole
Client proteins

ABSTRACT

Although hepatocellular carcinoma (HCC)-related mortality has increased over the past decades, treatment options are still very limited, underlining the need for developing new therapeutic strategies. The molecular chaperone heat shock protein 90 (Hsp90) plays a key role in post-translational maturation of many oncogenic client proteins that are important for survival and proliferation of cancer cells. Thus, inhibitors of Hsp90 are promising targets for many cancer types. In this study, 15 diarylpyrazole compounds were screened against MCF7 and HepG2 cell lines. Compound **8**, which contained a thiophene group, demonstrated the highest antiproliferative activity against HepG2 cells having an IC_{50} of 0.083 μM. Four additional diarylpyrazoles, each containing a thiophene group, were prepared and screened for antiproliferative activity. None of these four compounds exhibited superior activity to compound **8** on HepG2 cells. Therefore, compound **8** was selected for further *in vitro* assays. Cell cycle arrest was observed at the G2 phase in compound **8**-treated cells. Compound **8** also caused a 7.7-fold increase in caspase-3. These results confirm the apoptotic effect of compound **8** on HepG2 cells. Moreover, compound **8** inhibited Hsp90 (IC_{50} = 2.67 ± 0.18 μM) in an *in vitro* assay and caused a 70.8% reduction in Hsp90 levels in a HepG2 cell-based assay. Additionally, compound **8** caused significant reduction in the levels of Hsp90 client proteins (Akt, c-Met, c-Raf, and EGFR) and a 1.57-fold increase in Hsp70. Molecular docking studies were also performed to predict the binding mode of compound **8** and followed by molecular dynamics simulations to give further insights into the binding mode of **8**.

1. Introduction

Liver cancer or hepatocellular carcinoma (HCC) has the third highest mortality rate amongst cancer-related illnesses worldwide [1]. Although treatment modalities have remarkably improved over the past years, most patients with advanced HCC ultimately require surgery such as resection or orthotopic liver transplantation. Sorafenib, a non-selective multiple kinase inhibitor, is the only approved drug for advanced HCC. However, limited efficacy and *de novo* resistance to sorafenib, emphasize the urgent need for developing new therapeutics to treat the disease [2].

Given the intratumor heterogeneity of HCC, working on a single molecular target in a signaling pathway is not considered a practical approach and may explain the poor response to many emerging targeted therapies. Hence, a good target to work on is a one that may synchronize with or control several other downstream molecules implicated in carcinogenesis. Heat shock proteins (HSPs) are molecular chaperones that are constitutively expressed cellular proteins and guide the normal folding, disposition, and turnover of many of the key regulators of cell growth and survival [3]. These processes are achieved by multiple chaperone complexes acting in co-operation with several co-chaperones. The intracellular levels of these molecular chaperones increase in response to various stresses such as heat, electric shock, chemicals, toxins, and ischemia. These stresses can cause cellular protein denaturation and cell damage. In response to these stimuli, cells increase the level of HSPs to mediate protein refolding. Proteins that fail to refold properly are ubiquitinated and degraded by proteasomes. Newly synthesized proteins also need HSPs for proper folding and assembly [4]. The molecular chaperone ATP-dependent heat shock protein 90 (Hsp90) is the most common among the family of HSPs. It plays

* Corresponding authors.
E-mail addresses: samy.mohamady@bue.edu.eg (S. Mohamady), yasmeen.attia@bue.edu.eg (Y.M. Attia).

https://doi.org/10.1016/j.bioorg.2019.103433
Received 22 April 2019; Received in revised form 9 October 2019; Accepted 11 November 2019

a key role in post-translational maturation, proper folding, and activation of over a five hundred client proteins [5]. Many of these proteins are important oncogenic transcription factors, steroid receptors, and protein kinases. Hsp90 is abundant in normal cells and constitute up to 1–2% of total cell proteins. This percentage increases up to three-fold in cancer cells [6]. Cancer cells utilize Hsp90 to chaperone mutated and overexpressed oncogenic client proteins to protect them from misfolding and degradation. Thus, inhibition of Hsp90 can result in simultaneous and collective disruption of oncogenic signal transduction pathways and eradication of these oncogenic client proteins via ubiquitin-proteasome activation and, ultimately, apoptosis of the cancer cells [7]. Drugs that target Hsp90 were found to be selective for cancer cells over normal cells [7,8]. This is attributed to the fact that Hsp90 derived from tumor cells was found to be present in the active ATP consuming form, while those from normal tissues are in dormant state [8]. These drugs, whether used as monotherapy or in combination with other chemotherapeutic agents, are considered as a promising treatment strategy for various types of malignancy.

At the molecular level, Hsp90 is a flexible homodimer. Each monomer consists of three domains, an *N*-terminal ATP and drug binding domain, a middle domain for client protein and co-chaperone binding and ATP-hydrolysis, and a *C*-terminal domain containing sites for dimerization. There are two main Hsp90 isoforms, Hsp90α and Hsp90β. Hsp90α is stress-inducible, while Hsp90β is constitutive [9].

Interest in the development of selective Hsp90 inhibitors has grown rapidly over the last two decades [10]. More than 20 Hsp90 inhibitors are currently in various phases of clinical trials. So far, none of these inhibitors has been commercialized [11]. Most of the Hsp90 inhibitors target the *N*-terminal domain at the ATP-binding site, preventing ATP hydrolysis necessary for proper Hsp90 functioning and ensuing proteasomal degradation of client proteins leading to apoptosis of cancer cells [12]. These Hsp90 inhibitors are usually classified according to chronological evolution into two generations. The benzoquinoid ansamycin antibiotic geldanamycin (GA, Fig. 1) is the vanguard of the first generation and was first described as an Hsp90 inhibitor in mid 1990s [13]. GA blocks ATP from binding to the *N*-terminal pocket by mimicking the 3D structure that ATP adopts in the active site of the *N*-terminal pocket [14]. In an effort to combat GA side effects such as hepatotoxicity and lower aqueous solubility, three derivatives of GA were developed; 17-allylamino-demethoxy geldanamycin (17-AAG, Tanespimycin) was developed to reduce hepatotoxicity, while 17-dimethylaminoethylamino-17-demethoxy geldanamycin (17-DMAG) and IPI-504 (retaspimycin) were developed as water soluble GA derivatives with lower hepatotoxicity. Unfortunately, none of these compounds passed Phase II clinical trials [15]. The failure of these compounds has stimulated the quest for other structural scaffolds with better pharmacological and safety profiles. This resulted in the development of the second generation Hsp90 inhibitors; these are synthetic compounds that can be broadly categorized into three main categories, the purine family [16], the pyrazole family [17], and the isoxazole family (Fig. 1) [18].

There is increasing interest in Hsp90 as a target for treating HCC. The lack of clinical efficacy of current Hsp90 inhibitors [19] prompted us to search for novel Hsp90 inhibitor chemotypes and investigate their anti-HCC potential *in vitro*. Here we report on the discovery of 5-aryl-3-thiophen-2-yl-1H-pyrazoles as novel Hsp90 inhibitors possessing potent Hsp90 inhibitory activity in HepG2 cells.

2. Results and discussion

2.1. Chemistry

Compounds **1, 2, 3, 4, 5, 6, 7,** and **8** were previously prepared according to our reported procedure (Table 1 entries 1–8) [20]. Using the same reaction methodology, compounds **9, 10,** and **11** were prepared by heating a mixture of the corresponding aryl ketone and 1.2 equiv aryl hydrazone in ethanol in presence of catalytic amounts of hydrochloric acid for 1 h followed by the addition of 4 equiv DMSO and 0.1 equiv iodine and reflux for 16 h. (Table 1 entries 9–11)

The reverse method, whereby the hydrazone of the ketone is condensed with an aryl aldehyde was used for the preparation of compounds **12, 13, 14, 15, 16, 17, 18** (Table 2 entries 1–7).

Compound **19** was prepared according to a variant of our general synthetic protocol by refluxing 4-amino-acetophenone and 1.2 equiv. benzalhydrazone in ethanol in presence of catalytic amounts of HCl and H_2SO_4 for 100 h (Scheme 1).

3. Biological evaluation

3.1. Effect of compounds on cell viability

Initially, 15 diarylpyrazole compounds were screened for their potential anticancer activity on two cancer cell lines; MCF7 and HepG2. Table 3 shows the IC_{50} values of these 15 compounds (**1–9**, **12–16**, and **19**) on both MCF7 and HepG2 using Erlotinib as reference. The presented results showed a promising antiproliferative potential for **8**, particularly on HepG2 cell line which was, therefore, selected as lead for further optimization.

It was observed from the biological data given in Table 3 that the most potent analog was compound **8** which carries 2-thienyl moiety. By comparing the activities of compounds **1**, **7**, and **8**, it was clear that 2-thienyl moiety contribute well to the activity. It was also observed that the presence of 3-OCH_3, 3-OH, or 4-halogeno substitution contributes to the biological activity. For example, compound **5** contains 4-CF_3 and 3,4-dimethoxy (IC_{50} = 0.52 ± 0.01 μM) , compound **9** possesses 3- and 4-OH (IC_{50} = 0.57 ± 0.01 μM), and compound **15** possesses 4-Br and 4-CF_3 (IC_{50} = 0.74 ± 0.03 μM) (Table 3). Therefore, four additional pyrazole compounds were prepared in which the thiophene group was kept and the other substituents were 3-OH, 4-CF_3, 3,4-dimethoxy, and 2-fluoro-4-OCH_3 respectively (Table 4). The four compounds were then tested against HepG2 cells (Table 4). None of the tested compounds gave superior activity to **8**. Thus, further biological assays were performed on **8**.

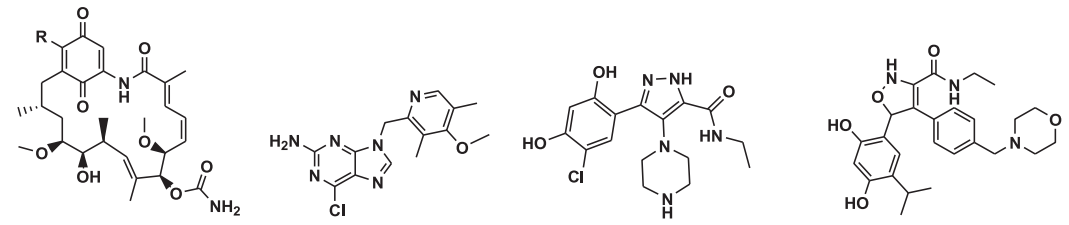

Fig. 1. Structure of some natural and synthetic Hsp90 inhibitors.

Table 1
Synthesis of 3,5-diaryl pyrazoles from aryl ketones and aldehyde hydrazones

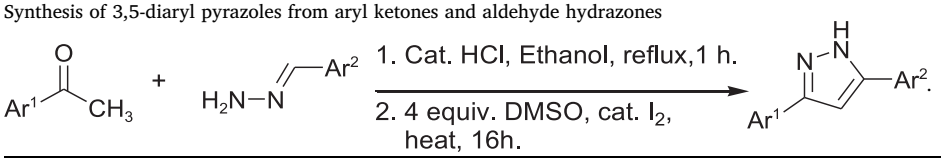

Entry	Ar^1	Ar2	Product	Yield (%)
1	h-	Ph-	**1**	85
2		Ph-	**2**	73
3			**3**	71
4		Ph-	**4**	77
5			**5**	86
6		Ph-	**6**	90
7		Ph-	**7**	78
8			**8**	74
9			**9**	71
10			**10**	75
11			**11**	82

3.2. Effect of 8 on cell cycle

As shown in Fig. 2, cell cycle analysis showed that **8** caused cell cycle arrest at the G2 phase where the number of cells treated with **8** were 2.3-fold higher in the G2 phase compared to control. Moreover, treatment with **8** caused a 6.2-fold increase in the cells in pre-G1. Early and late apoptotic cells were also 3.3- and 21-fold higher in **8**-treated cells, as compared to control, respectively. Additionally, necrotic cells were 4.2-fold higher in treated cells compared to control. These results strongly suggest that compound **8** has an antiproliferative effect on HepG2 cells.

Table 2
Synthesis of 3,5-diaryl-pyrazoles using ketone hydrazones and aryl aldehydes.

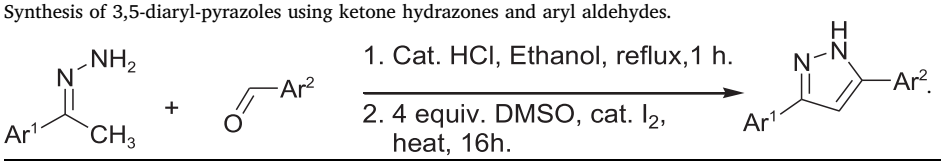

	Ar^1	Ar^2	Product	Yield (%)
1	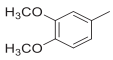	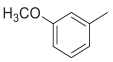	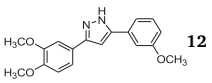 **12**	81
2	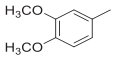		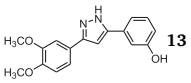 **13**	81
3		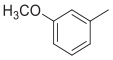	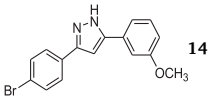 **14**	90
4			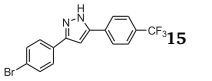 **15**	92
5			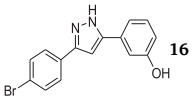 **16**	92
6	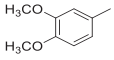		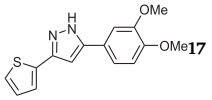 **17**	80
7		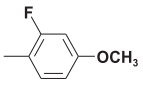	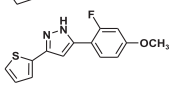 **18**	80

3.3. Effect of 8 on caspase-3 levels

In order to further confirm the apoptotic potential of **8** on HepG2 cells, the level of the primary executioner caspase, caspase-3, was evaluated and compared to that of erlotinib. As shown in Fig. 3, caspase-3 was 7.7-fold higher in **8**-treated HepG2 cells compared to control. Erlotinib, on the other hand, caused almost one-fold higher expression of caspase-3 compared to **8**. These results further confirm the apoptotic potential of **8**.

3.4. Effect of 8 on Hsp90

In order to investigate the inhibitory potential of **8** on Hsp90 (*C*-terminal domain), an *in vitro* enzyme inhibition assay was performed where the IC_{50} calculated was found to be 2.67 ± 0.18 μM. Moreover, in order to investigate whether this effect could be extrapolated to HepG2 cells, a cell-based ELISA assay was performed to estimate the level of Hsp90 after treatment with **8**. As shown in Fig. 3, HepG2-treated cells showed a 70% reduction in Hsp90, as compared to control untreated cells.

3.5. Effect of 8 on Hsp70

Hsp90 inhibition is accompanied by the induction of the chaperone Hsp70 which is considered a molecular signature for both targets. Hence, the effect of **8** on Hsp70 was investigated in HepG2 cells. As shown in Fig. 3, Hsp70 level was 1.6-fold higher in **8**-treated HepG2 cells compared to untreated cells. These results further confirm inhibition of Hsp90 by **8**. Despite the fact that a correlation between an increase in Hsp70 levels and Hsp90 inhibition was reported in many previous studies [21,22], the study of Wang et al. [23], suggested that the increase in Hsp70 could be related to stress induced in cells which may or may not be due to Hsp90 inhibition. Accordingly, Hsp70 alone might not be a reliable tool to validate Hsp90 inhibition and hence investigating the effect of **8** on client proteins was also performed.

3.6. Effect of 8 on Hsp90 client proteins

Hsp90 is responsible for the functioning of a number of client proteins that are known to control cancer development and progression. So, inhibition of Hsp90 will ultimately cause degradation of the pro-survival client proteins. Investigation of the effect of **8** on four Hsp90

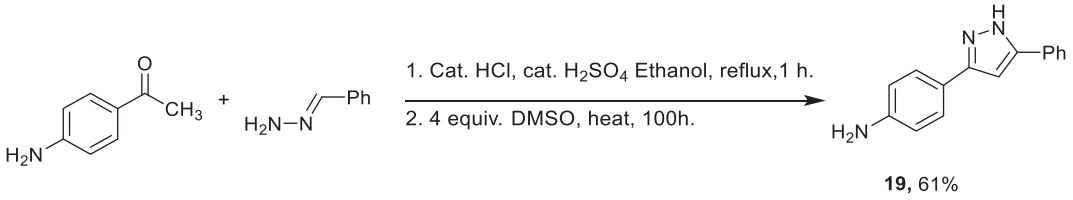

19, 61%

Scheme 1. Synthesis of **19**.

Table 3
In vitro antiproliferative potential of the newly synthesized first series of compounds against MCF7 and HepG2 cell lines. Data are presented as mean ± S.D. of IC_{50} values.

Compound	Structure	IC50 (μM)	
		MCF7	HepG2
1	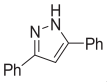	12.85 ± 0.76	97.52 ± 0.26
2	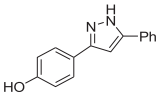	25.36 ± 1.61	8.57 ± 0.41
3	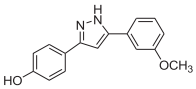	19.82 ± 1.1	1.20 ± 0.03
4	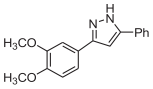	2.64 ± 1.2	11.62 ± 0.24
5	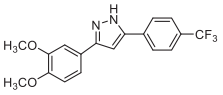	0.14 ± 0.002	0.52 ± 0.01
6	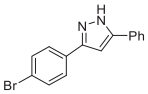	1.21 ± 0.06	7.06 ± 0.23
7	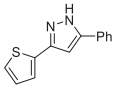	2.11 ± 0.41	0.87 ± 0.02
8	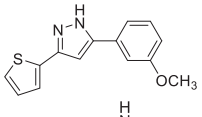	0.13 ± 0.006	0.083 ± 0.003
9	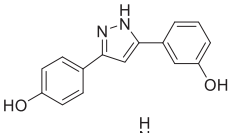	0.11 ± 0.002	0.57 ± 0.01
12	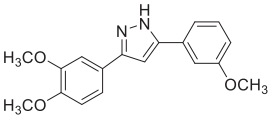	19.17 ± 0.64	119.09 ± 3.7
13	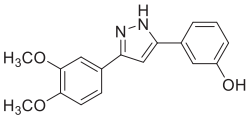	137.12 ± 3.8	152.29 ± 5.1
14	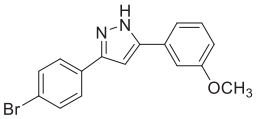	1.00 ± 0.01	2.65 ± 0.11
15	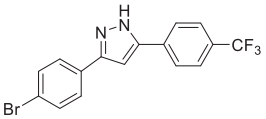	2.24 ± 0.61	0.74 ± 0.03
16	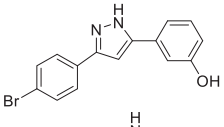	16.30 ± 0.32	5.20 ± 0.25
19	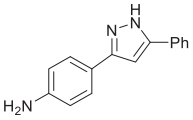	0.94 ± 0.03	6.15 ± 0.21
Erlotinib (Reference)		1.14 ± 0.01	0.87 ± 0.04

Table 4
In vitro antiproliferative potential of the second series of compounds against HepG2 cell line. Data are presented as mean ± S.D. of IC_{50} values.

Compound	Structure	IC_{50} (uM)
		HepG2
10	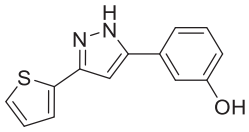	5.15 ± 0.21
11	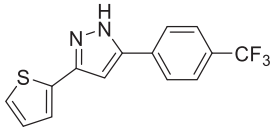	1.66 ± 0.08
17	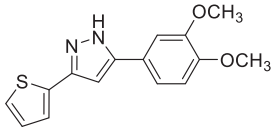	9.02 ± 0.28
18	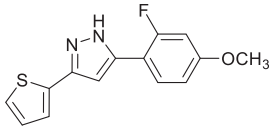	3.25 ± 0.11
Erlotinib (Reference)		1.94 ± 0.06

client proteins (Akt, c-Met, c-Raf, and EGFR) was performed in order to examine whether **8** triggered their degradation in HepG2 cells. Their levels were all significantly decreased after treatment reaching 87, 90, 77, and 90% for Akt, c-Met, c-Raf, and EGFR, respectively (Fig. 4). These findings suggest a potential degradation of the aforementioned client proteins, and further validate Hsp90 inhibition by **8**.

3.7. Molecular docking

A molecular docking study was carried out in order to predict the binding mode of compound **8** inside Hsp90 C-Terminal Domain (CTD). The CTD of human Hsp90 alpha (PDB ID: 3Q6M) [24] was used as a receptor model for docking. In this crystal structure, missing loop in Hsp90 alpha (PDB ID: 3Q6M) (616–629) was modeled using Modeller [25] software which was implemented through "Model Loops/Refine Structure" utility in UCSF chimera 1.13.1 [26]. Docking search space was assigned to enclose the interface between the CTD of the two chains, A and B, (651–698) [27]. Docking simulations were conducted using two docking engines implementing two different search algorithms (systematic for FRED and stochastic for AutoDock vina) and scoring functions (Chemgauss4 for FRED [28] and tuned X-score, combining knowledge-based potentials and empirical scoring functions, for AutoDock vina [29]). Since the pyrazole hydrogen is tautomeric, in each docking run, the two ligand pyrazole tautomers, 3-thiophen-2-yl and 5-thiophen-2-yl, were considered, and are referred to as tautomer1 and tautomer2, respectively, throughout the text. Based on the docking scores, three poses of docking results were chosen to be subjected to molecular dynamics (MD) simulations. For FRED results, two types of binding modes were observed occupying 100% and 60% for tautomer1 and tautomer2, respectively. For vina results, one pose occupied 40% for tautomer1 which is similar to that of FRED, hence it was cancelled for being redundant with FRED result for tautomer1, and the other occupied 30% for tautomer2 and subjected to MD simulations. The three binding modes are depicted in Fig. 5B. Tautomer1 and tautomer2 poses of FRED, referred to as t1f and t2f, show a hydrogen bond

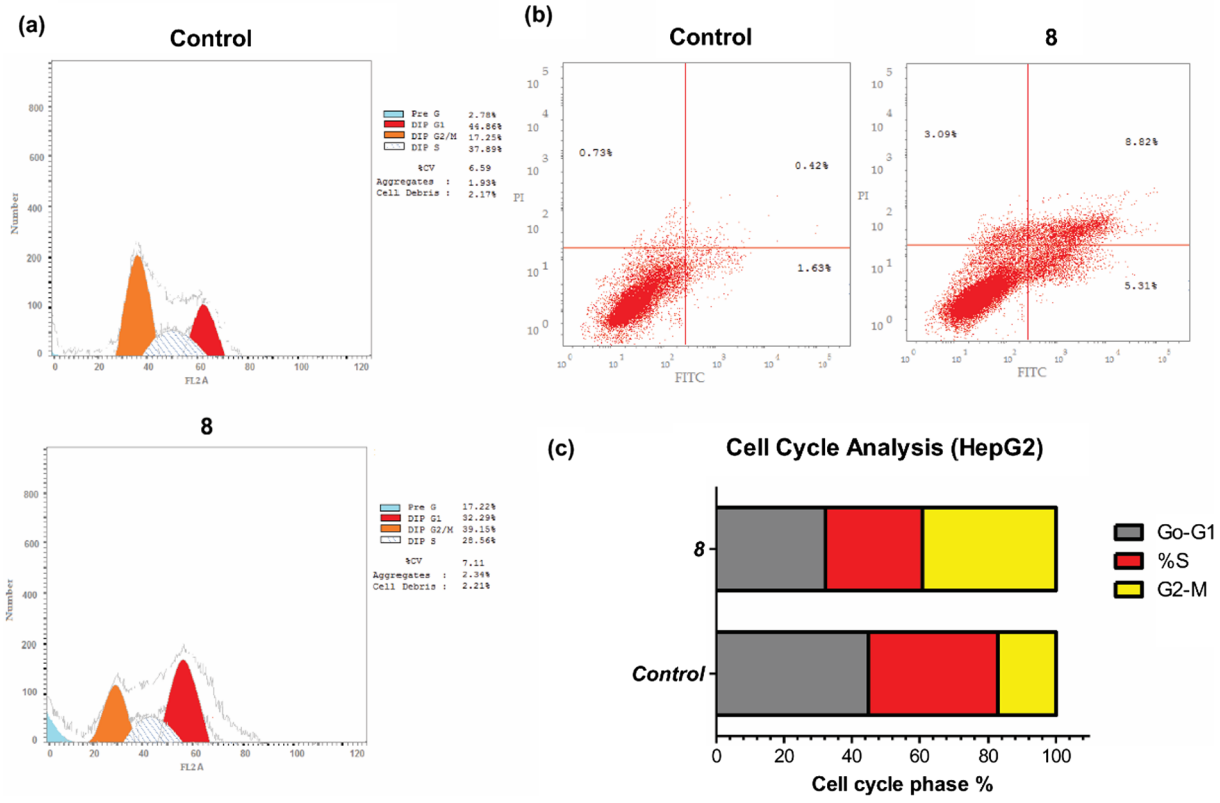

Fig. 2. Effect of **8** on cell cycle progression in HepG2 cell line. **(a)** Representative histograms for the effect of **8** on cell cycle phases compared to control. **(b)** Control and **8**-treated HepG2 cells double stained with Annexin V-FITC and propidium iodide (PI) and analyzed by flow cytometry showing living (bottom left), necrotic (top left), early apoptotic (bottom right), and late apoptotic (top right) cells. **(c)** Stacked bar chart representing different percentages of cells in each stage of cell cycle after treatment with 8 compared to control.

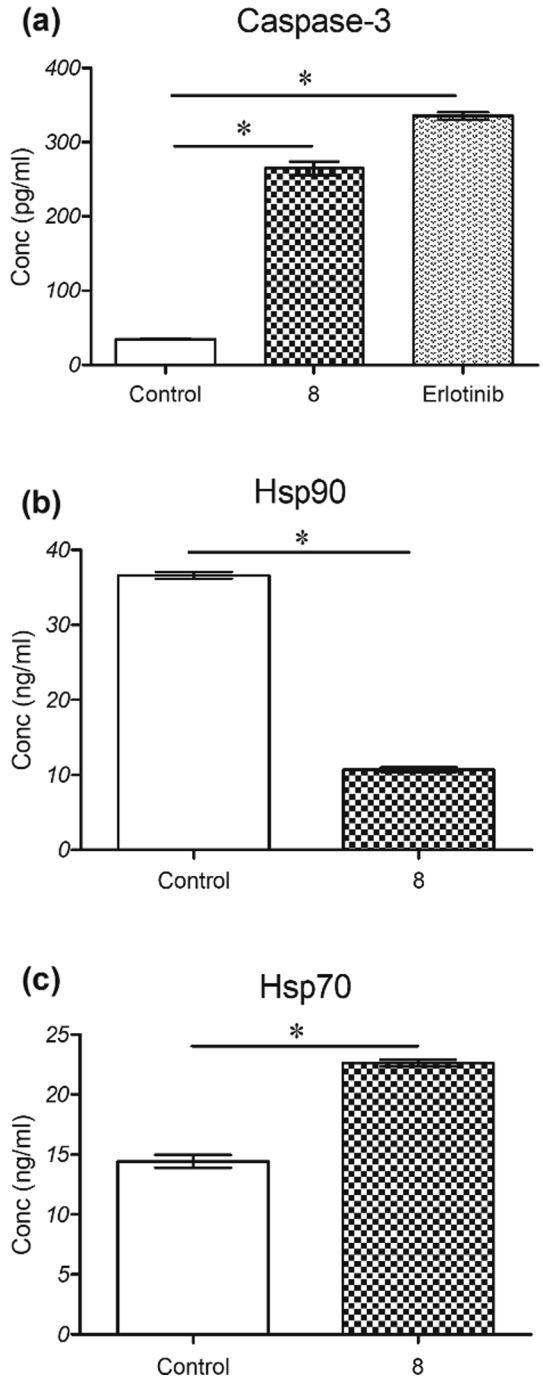

Fig. 3. Effect of **8** on caspase-3, Hsp90, and Hsp70 levels. (a) Caspase-3, (b) Hsp90, and (c) Hsp70 protein levels were determined in **8**-treated HepG2 cells. Protein levels were estimated using ELISA. Values are presented as means ± S.D. from three independent experiments performed in triplicates. *P < 0.05 significant from control untreated or erlotinib-treated cells using one-way ANOVA followed by Bonferroni post hoc test for caspase-3 and Student's *t* test for Hsp90 and Hsp70.

between the nitrogen of the pyrazole ring, which acts as a hydrogen bond acceptor, and the guanidine moiety of arginine 690 amino acid of chain B, which acts as a hydrogen bond donor, with docking scores of −11.2470 and −10.5955, respectively. Tautomer2 pose predicted by vina, referred to as t2v, shows no hydrogen bonds with the protein, with free energy of −6.7 kcal/mol.

Molecular docking was followed by molecular dynamics (MD) simulations to give further insights into the binding mode of **8** and the tautomer with more time-evolution stable binding dynamics. The 2D interaction representations between protein and **8** tautomer1 and tautomer2 are depicted in Fig. S1–4.

3.8. Molecular dynamics

In order to gain more insight into the binding mode of **8** inside Hsp90 CTD, molecular dynamics simulations for each binding pose were carried out for 10 ns at NPT ensemble for minimization and equilibration purposes. Analyses of protein RMSD (Root Mean Square Deviation), RMSF (Root Mean Square Fluctuation) and Radius of gyration are depicted in Fig. 6. RMSD is a measure of structure stability. RMSD of the protein backbone (C_α, C and N) in the 3 dynamics runs show stability after 7 ns of the simulation with RMSD 3.97 ± 0.73, 4.24 ± 0.99 and 4.34 ± 0.99 Å (mean ± SD) for t1f, t2f and t2v, respectively (Table S1). High RMSD standard deviation (SD) is attributed to the highly flexible loops present in *N*-terminal of the protein and the flexible loops (616–629) modelled by Modeller software (Fig. 5A), which contributes to the fluctuation of RMSD throughout the simulation.

RMSF is a measure for per residue stability and protein local conformational changes during the simulation. Binding site amino acid residues (651–698 of chain B) show minimal RMSF which is an indication for relatively strong binding with **8** throughout the simulation and minimal local conformational change in the binding site. Residues with high RMSF (> 2 Å) showed to be terminal or far away from the binding site. *N*-terminal loops of the A and B protein chains (535–554) and the modelled loops (616–629) show very high RMSF, 6–12 Å, confirming our observation of their high RMSD SD due to these highly flexible loops (Fig. 6).

Radius of gyration (R_g) is an indicator of the compactness of the protein structure and a parameter for protein equilibrium conformation. As shown in Fig. 6, R_g values of t1f, t2f and t2v, were 43.260 ± 0.182, 43.264 ± 0.184 and 43.249 ± 0.183 Å (mean ± SD), respectively (Table S2). R_g is stable for each protein throughout the simulation, hence, no major conformational changes occur during the simulation, and this is consistent with our knowledge that major protein conformational changes rarely occur in the nanosecond time range.

RMSD analysis of each of the **8** tautomers through evolution of simulation time revealed that t2v (5-thiophen-2-yl tautomer) has less RMSD than t1f (3-thiophen-2-yl tautomer) and t2f in the three simulations as shown in Fig. 7. The relatively high RMSD in both t1f and t2f indicates that the ligand abandons its starting position predicted by docking to a more stable binding pose.

A major finding in the binding interactions was observed that a hydrogen bond between the pyrazole N—H and Asp661 residue carboxylate was formed during the MD simulations that was not predicted by docking. Fig. 8 shows the total number of hydrogen bonds formed between the ligand and the protein vs the number of hydrogen bonds formed between the ligand and Asp661 (Table S3), which indicates the Asp661 hydrogen bond to be the driving force for such binding.

In Fig. 9, the last snapshot of the dynamics simulations, after 10 ns, for the three proteins is depicted along with the starting docking pose. It confirms the stable binding mode of compound **8** inside the binding pocket with the hydrogen bond between pyrazole N—H of **8** and carboxylic group of Asp661 being the main driving force for binding.

In conclusion, the hydrogen bond between **8** and Asp661 carboxylic group is the main interaction responsible for binding between **8** and Hsp90 CTD. From molecular dynamics simulations, it is concluded that Asp661 is responsible for the hydrogen bond with **8** not Arg690 predicted by docking (Supplementary information, videos 1, 2 and 3). Video 1, video 2 and video 3 trajectory analysis of t1f, t2f and t2v, respectively, show the stable binding due to the hydrogen bonding interaction with the key binding residues (Asp661) with less deviation of t2v.

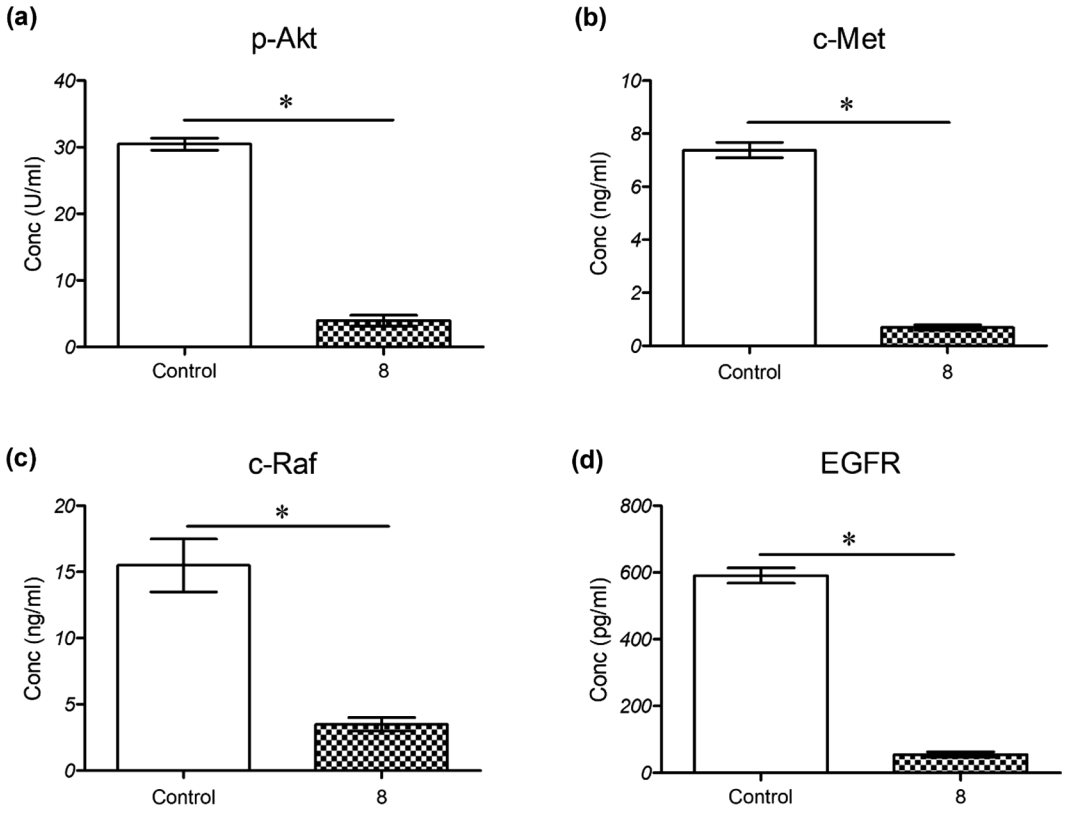

Fig. 4. Effect of **8** on HSP90 client proteins. Protein levels of (a) p-Akt, (b) c-Met, (c) c-Raf, and (d) EGFR were estimated in **8**-treated HepG2 cells. Protein levels were estimated using ELISA. Values are presented as means ± S.D. from three independent experiments performed in triplicates. *P < 0.05 significant from control untreated cells using Student's *t* test.

4. Experimental

4.1. General

All reagents and solvents were purchased from commercial suppliers and used without purification unless stated otherwise. Chemical shifts (δ) for ^{1}H NMR spectra in acetone-d_6 are reported in ppm relative to acetone-d_6 residual solvent protons (δ 2.05). Chemical shifts for ^{13}C NMR spectra run in acetone-d_6 are reported in ppm relative to the solvent residual carbon (δ 30.8). Peaks in NMR spectra are described as follows: singlet (s), broad singlet (bs), doublet (d) triplet (t) apparent doublet (appd), apparent triplet (appt), doublet of doublets (dd). Samples for high resolution positive ion electrospray ionization mass spectrometry (HRMS-ESI^{+}) were prepared in 1:1 CH_3CN/H_2O + 0.2% formic acid. Melting points are measured using Stuart SMP 30 and are uncorrected.

4.2. General method for the synthesis of compounds **17** and **18**

To a mixture of 2-acetyl-thiophene hydrazone (1.5 mmol, 210 mg) and the corresponding aldehyde (1.8 mmol) in ethanol (10 mL), added HCl (75 µL). The reaction mixture was refluxed for one hour, then DMSO (6 mmol, 425 µL) and iodine (0.15 mmol, 38 mg) were added. The reaction mixture was refluxed for 16 h, cooled to room

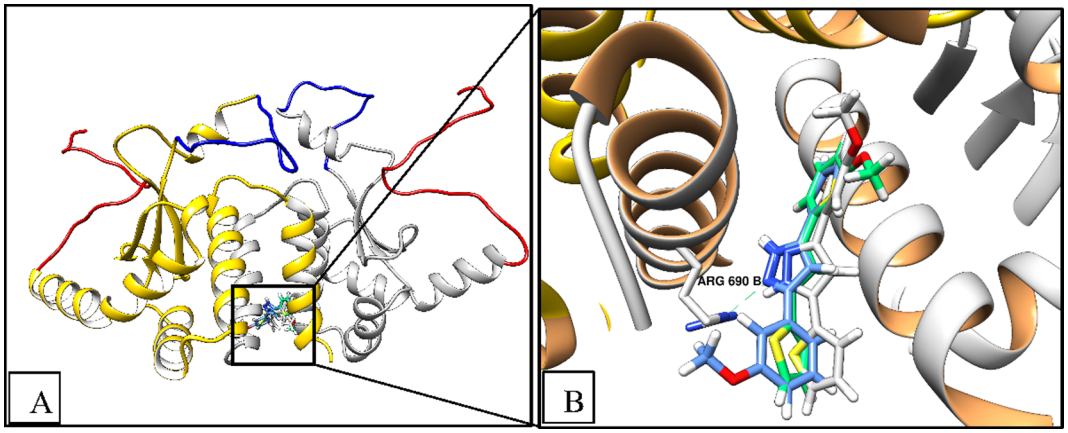

Fig. 5. (A) CTD of Hsp90 (3q6m) with the flexible *N*-terminal (red) and the loops modelled with Modeller software (blue). (B) Molecular docking results showing the two binding poses predicted by FRED (green for t1f and blue for t2f) and AutoDock vina (grey for t2v). The docked pose predicted by FRED shows a hydrogen bond between the pyrazole nitrogen and Arginine 690 in chain B. (Chain A is depicted in gold and chain B in grey).

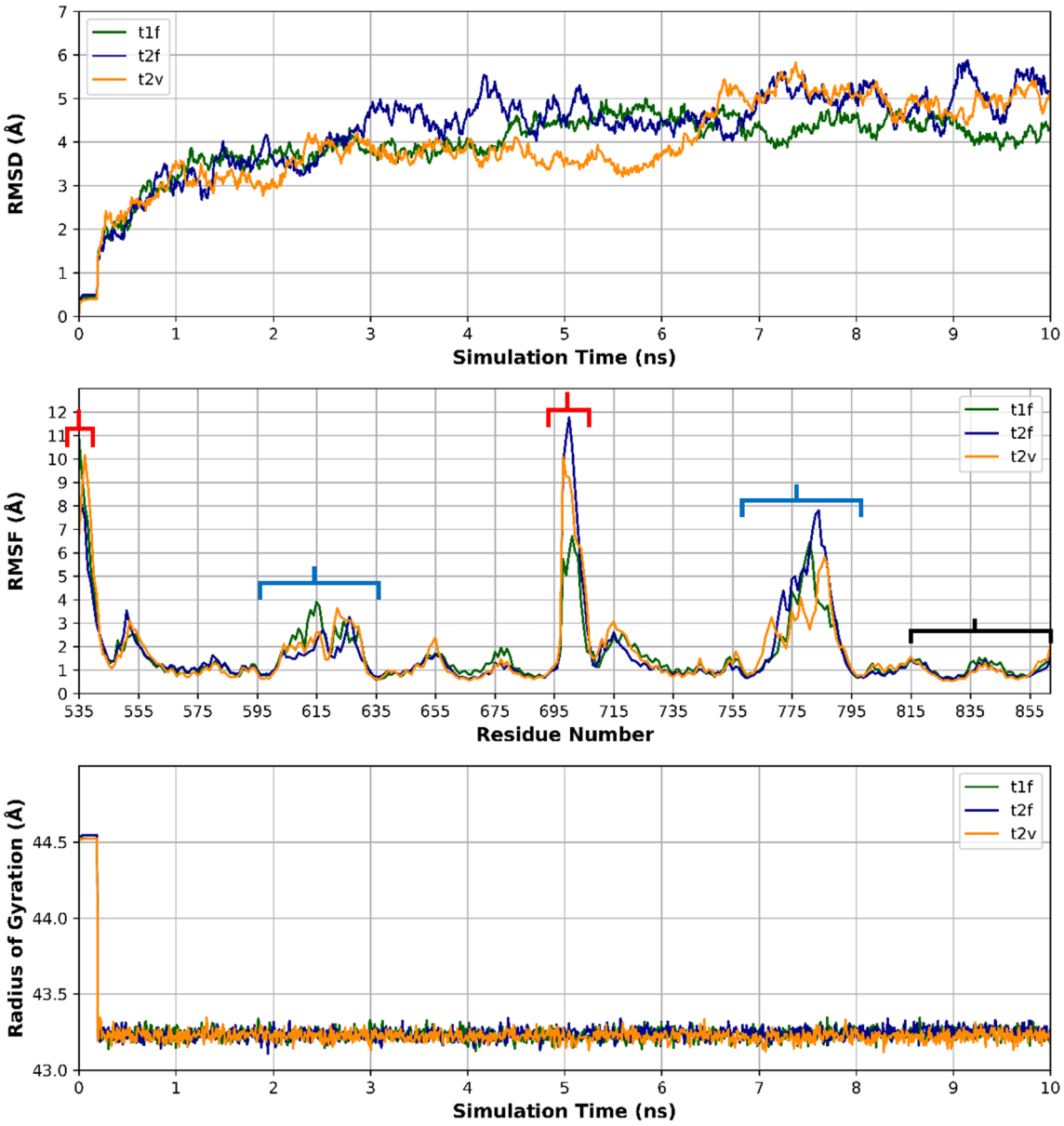

Fig. 6. RMSD (top), per residue RMSF (middle) and Radius of gyration (bottom) of the three protein structures (t1f, t2f and t2v). RMSF x-axis depicts the number of protein chain A 163 residues (535–697) and chain B 165 residues (698–862). Dark green, dark blue and dark orange for t1f, t2f and t2v, respectively. *N*-terminal (red braces) and modelled (blue braces) highly flexible loops of chains A and B show high RMSF (middle) and contributes to the RMSD (top) fluctuation. The binding site of chain B (black braces) shows low RMSF < 2 which is an indication for relatively strong binding with 8 throughout the simulation and minimal local conformational change in the binding site.

temperature, quenched with 5% aqueous sodium thiosulfate (ca 30 mL), and extracted with EtOAc (3 × 20 mL). The combined EtOAc extracts were washed with water (1 × 20 mL), dried over anhydrous magnesium sulfate and concentrated by rotary evaporation. The crude product was purified by column chromatography using a gradient of 30–50% EtOAc-Hexane. The desired fractions were pooled, concentrated and vacuum dried.

4.3. 5-(3,4-dimethoxyphenyl)-3-(thiophen-2-yl)-1H-pyrazole (17)

Yellowish white solid. 343 mg, 80%, Mp 159-160 °C. ^{1}H NMR (300 MHz, acetone-d_6): δ 12.41 (bs, 1H), 7.36-7.44 (m, 4H), 7.09 (t, J = 3.6 Hz, 1H), 7.03 (d, J = 8.2 Hz, 1H), 6.92 (s, 1H), 3.89 (s, 3H), 3.85 (s, 3H); ^{13}C NMR (75 MHz, DMSO-d_6): δ 149.4,147.2, 144.0, 137.5, 128.0, 125.0, 123.9, 122.3, 118.1, 112.4, 109.4, 99.2, 55.9; HRMS-ESI+ (*m/z*): $[M+H]^+$ calculated for $C_{15}H_{15}O_2N_2S$, 287.0849; found, 287.0848.

4.4. 5-(2-fluoro-4-methoxyphenyl)-3-(thiophen-2-yl)-1H-pyrazole (18)

Yellow solid, 329 mg, 80%, Mp 138-140°C. ^{1}H NMR (300 MHz, acetone-d_6): δ 12.4 (s, 1H), 7.81 (t, J = 9.2 Hz, 1H), 7.44 (d, J = 4.6 Hz, 1H), 7.39 (d, J = 4.9 Hz, 1H), 7.08 (d, J = 3.6, 5.3 Hz, 1H), 6.84–6.88 (m, 3H); ^{13}C NMR (75 MHz, DMSO-d_6): δ 160.5; 159.2 (d, J = 243.1 Hz), 146.6, 137.4, 136.8, 128.4, 127.6, 124.6, 123.7, 111.0, 102,1 (d, J = 26.8 Hz); 101.1, 55.7; ^{19}F NMR (282 MHz, acetone-d_6): δ-114.2 HRMS-ESI+ (*m/z*): $[M+H]^+$ calculated for $C_{14}H_{12}ON_2SF$, 275.0649; found,. 275.0647.

4.5. General method for the synthesis of compounds 10 and 11

To a mixture of 2-acetyl-thiophene (1.5 mmol, 189 mg) and the corresponding aldehyde hydrazone (1.8 mmol) in ethanol (10 mL), was added HCl (75 μL). The reaction mixture was refluxed for one hour,

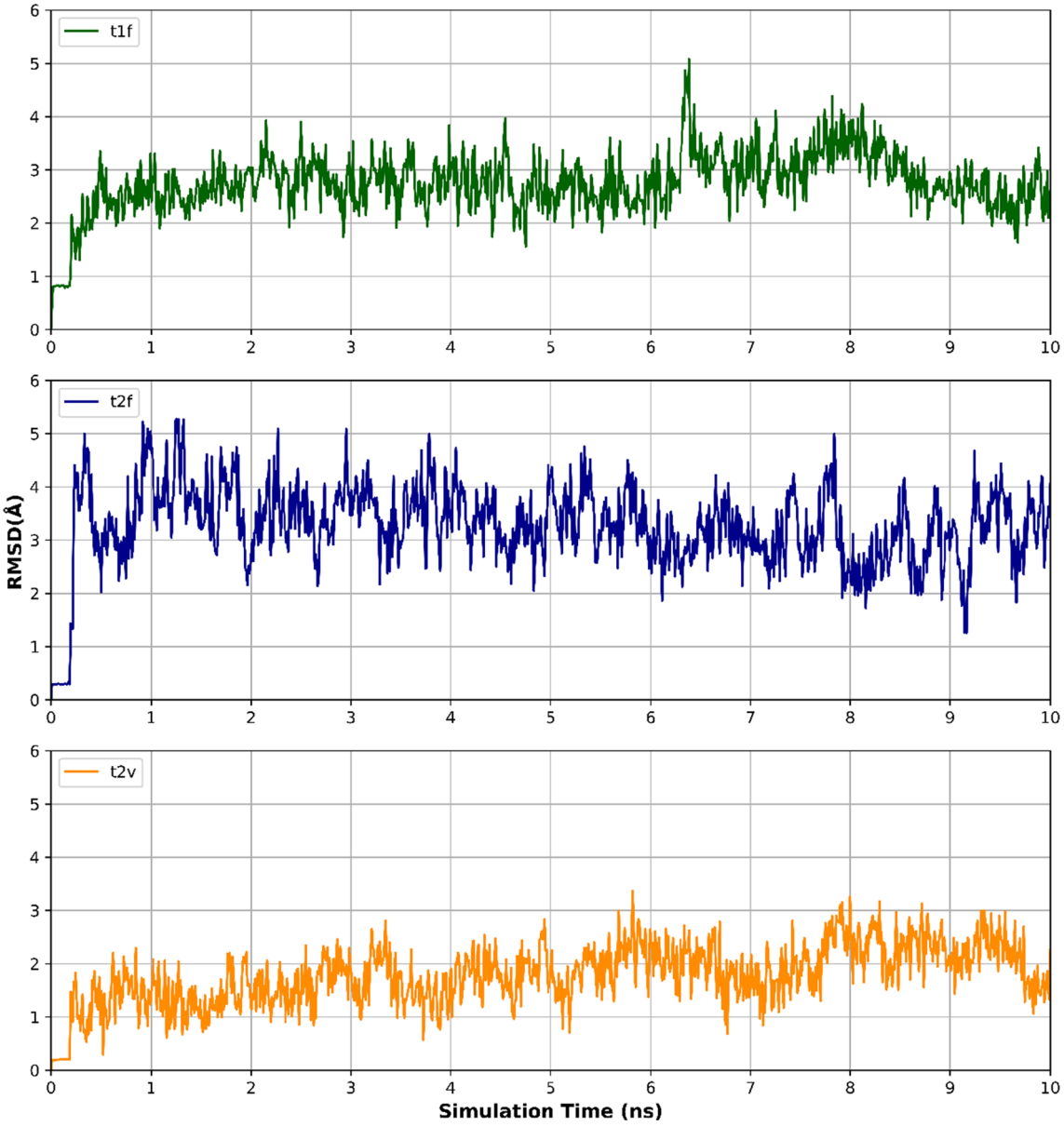

Fig. 7. RMSD analysis of **8** tautomers with each protein through the simulation time.

then DMSO (6 mmol, 425 µL) and iodine (0.15 mmol, 38 mg) were added. The mixture was refluxed for 16 hours, cooled to room temperature, quenched with 5% aqueous sodium thiosulfate (ca 30 mL), and extracted with EtOAc (3 × 20 mL). The combined EtOAc extracts were washed with water (1 × 20 mL), dried over anhydrous magnesium sulfate and concentrated by rotary evaporation. The crude product was purified by column chromatography using a gradient of 30–50% EtOAc-Hexane. The desired fractions were pooled, concentrated and vacuum dried.

4.6. 3-(3-(thiophen-2-yl)-1H-pyrazol-5-yl)phenol (**10**)

Yellow solid, 273 mg, 75%, Mp 179–181 °C. ^{1}H NMR (300 MHz, acetone-d_6): δ 12.45 (bs, 1H), 8.48 (bs, 1H), 7.43 (d, J = 3.6 Hz, 1H), 7.39 (d, J = 4.6 Hz, 1H), 7.22-7.28 (m, 3H), 7.08 (t, J = 4.6 Hz, 1H), 6.91 (s, 1H), 6.83 (d, J = 6.9 Hz, 1H); ^{13}C NMR (75 MHz, DMSO-d_6): δ 157.7, 146.8, 143.6, 136.9, 130.0, 127.6, 124.6, 123.7, 116.1, 115.3, 99.3; HRMS-ESI+ (m/z): $[M+H]^+$ calculated for $C_{13}H_{11}ON_2S$, 243.0587; found, 243.0584.

4.7. 3-(thiophen-2-yl)-5-(4-(trifluoromethyl)phenyl)-1H-pyrazole (**11**)

Yellow solid, 353 mg, 80%, Mp 224-226°C. ^{1}H NMR (300 MHz, acetone-d_6): δ 12.76 (bs, 1H), 8.10 (d, J = 6.9 Hz, 1H), 7.80 (d, J = 7.9 Hz, 1H), 7.50 (bs, 1H), 7.13 (bs, 1H); ^{13}C NMR (75 MHz, DMSO-d_6): δ 147.7, 142.4, 138.6, 133.3, 128.6, 128.1, 126.7, 126.5, 126.1, 125.4, 125.2, 124.4, 101.1; ^{19}F NMR (282 MHz, acetone-d_6): δ – 63.3 HRMS-ESI+ (m/z): $[M+H]^+$ calculated for $C_{14}H_{10}N_2SF_3$, 295.0511 ; found, 295.0512.

4.8. Cell lines and cell culture

MCF7, estrogen-dependent breast cancer cell line, and HepG2, hepatocellular carcinoma cell line, were obtained from the American Type Culture Collection (ATCC, VA, USA). Cells were cultured using Dulbecco's Modified Eagle Medium (DMEM; Invitrogen, Life Technologies, CA, USA) supplemented with 10% fetal bovine serum (FBS; GE Healthcare HyClone, WV, USA), streptomycin (100 µg/ml) and penicillin (100 units/ml) and incubated in 5% CO_2 at a temperature of 37 °C. Passaging was performed when cells were 80–90% confluent.

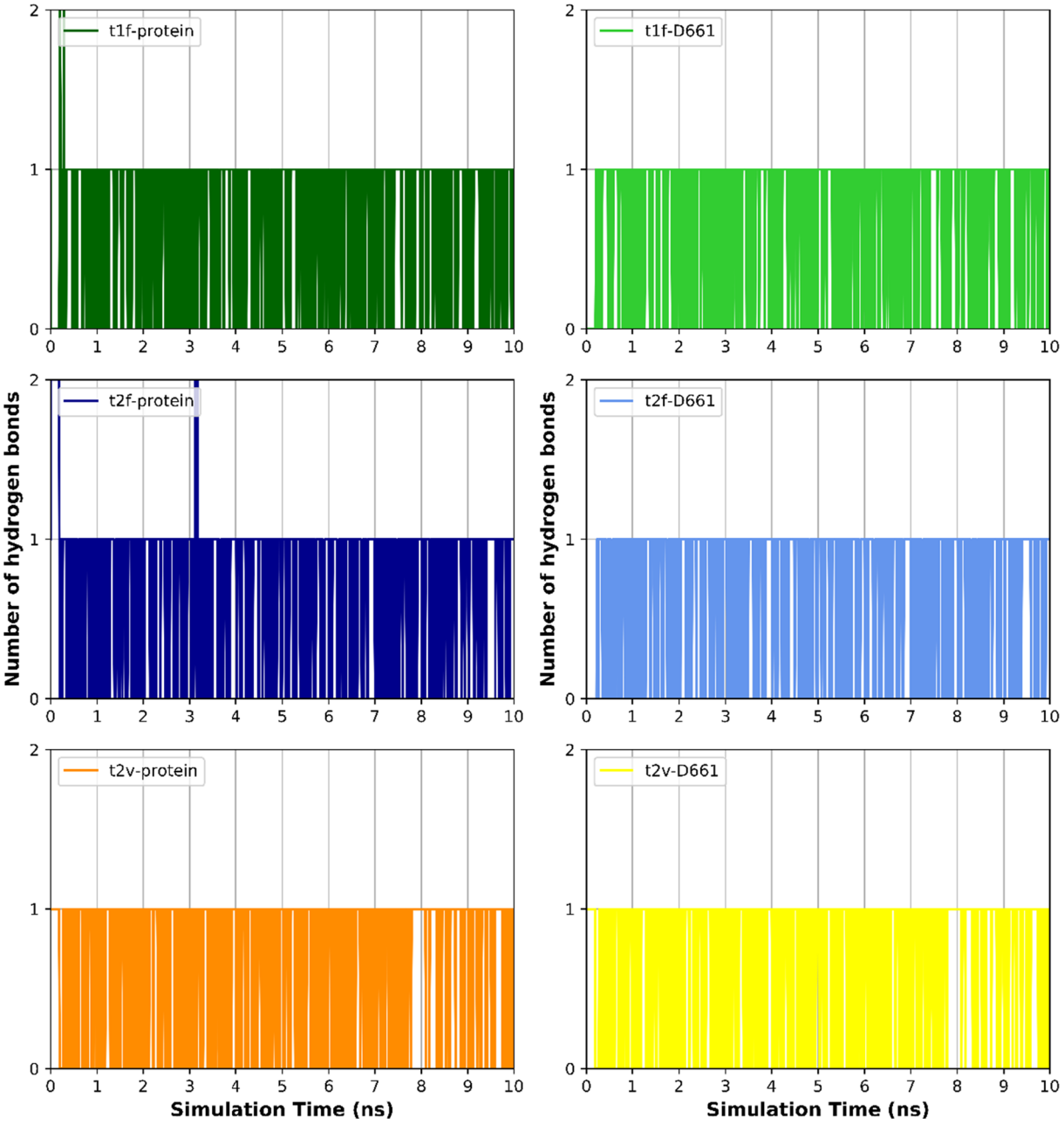

Fig. 8. Number of hydrogen bonds between **8** tautomers, and the three protein structures (left), and Asp661 (right), as a function of simulation time.

4.9. Cell viability assay

The first series of compounds were tested against both MCF7 and HepG2 cells. Following this screening step, optimization of compounds was performed where the second series was tested against HepG2 cells only. MCF7 and HepG2 cells were seeded in 96-well plates at a density of 1×10^4 cells/well. One day after seeding plates, MCF7 and HepG2 cells were treated with a 10 fold serial dilution (0.01–100 μM) of the first series; (compounds **1–9**, **12–16**, and **19**) or Dimethyl sulfoxide (DMSO; Sigma-Aldrich, St. Louis, MO, USA) as a vehicle representing the negative control. Erlotinib was used as a reference. As for the second optimized series of compounds (**10**, **11**, **17**, **18**), their cytotoxic effect was investigated against HepG2 cells only using their 10-fold serial dilutions (0.01–100 μM). Cytotoxicity assay of compounds belonging to both series was assessed using 3-(4,5-dimethylthiazol-2-yl)-2,5-diphenyltetrazolium bromide (MTT) reagent (Sigma-Aldrich, St. Louis, MO, USA). Briefly, cells seeded in 96-well plates were cultured overnight and on the next day, cells were treated with serial dilutions of the compounds besides DMSO. Then after seventy-two hours, 20 μl of 5 mg/ml MTT was added to each well then incubated for 2 h. The absorbance was then measured at 570 nm. The percentage of the absorbance at 570 nm in treated cells against control represented the cell viability. All experiments were performed in triplicates. Half-maximal inhibitory concentration (IC_{50}) was calculated using GraphPad Prism software, version 5.00 (GraphPad Software, CA, USA). For further cell cycle analysis and cell-based assays, HepG2 cells were treated with the IC_{50} of compound **8**.

4.10. Apoptosis assay using Annexin V/Propidium iodide staining

HepG2 cells cultured in six-well plates were treated with **8** for 48 hours. Then, the cells were fixed in cold ethanol for half an hour and stained with 5 μl Annexin V-FITC and 5 μl propidium iodide (PI) using an Annexin VFITC Apoptosis Detection Kit (BioVision, CA, USA). The

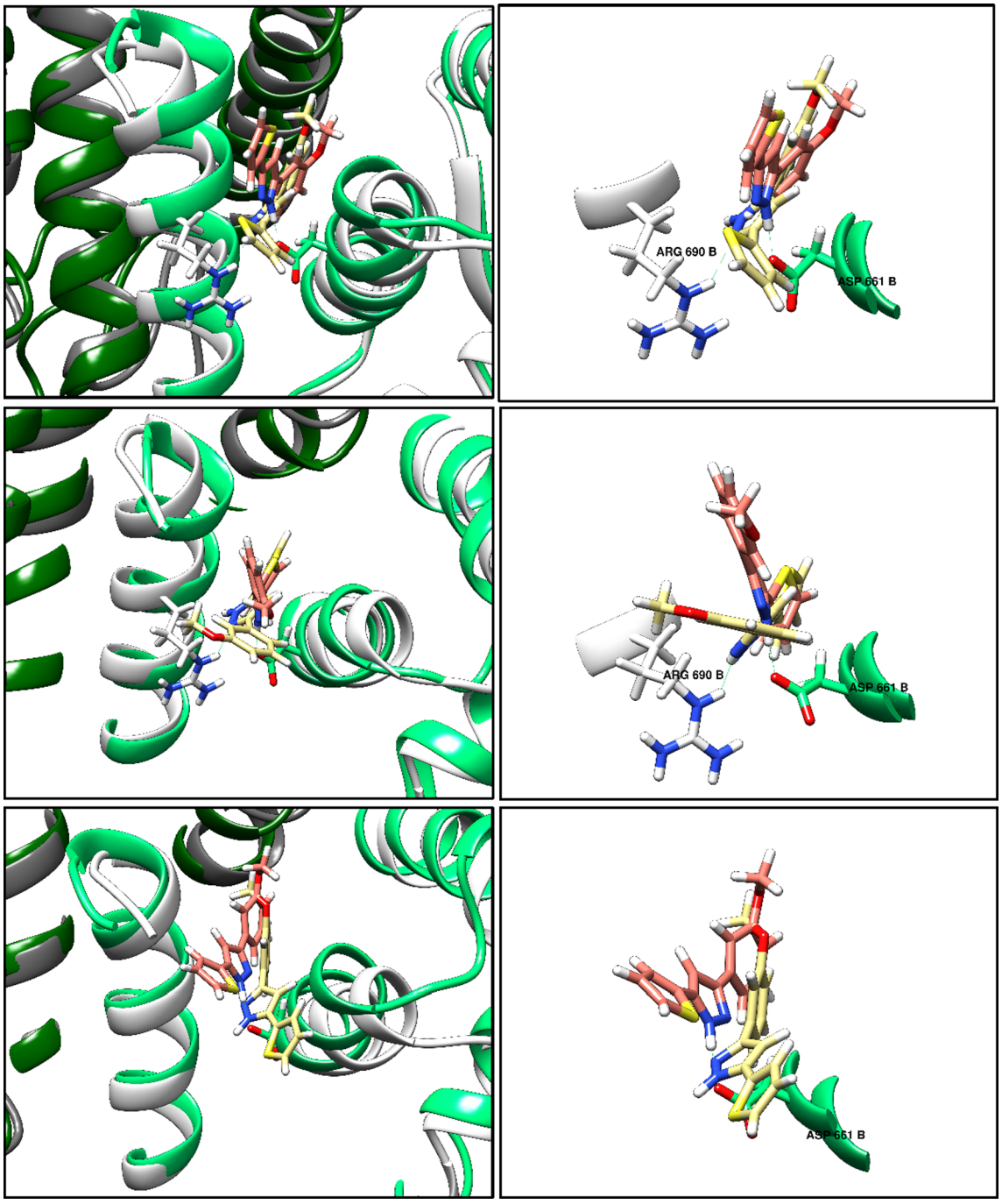

Fig. 9. Comparison between the starting protein structure (chain A in dark grey and chain B in white) with starting ligand pose (khaki) and the last snapshot after 10 ns molecular dynamics run (chain A in dark green and chain B in lime green) with ligand pose (salmon) for t1f (top), t2f (middle) and t2v (bottom). The three runs show a conserved hydrogen bond with Asp661 which is considered to be the driving force for protein ligand interaction.

cells were then placed at room temperature for 15 min in the dark then analyzed by a FACScan flow cytometer (Beckman Coulter, CA, USA). Apoptosis was evaluated in terms of the FITC-positive cells.

4.11. Cell cycle analysis

Forty-eight hours following the treatment of HepG2 with **8**, cells were trypsinized and washed with phosphate buffered saline (PBS), resuspended in cold methanol, and kept overnight at 4 °C. Collected cells were then resuspended in sodium citrate buffer together with RNase, and incubated at 37 °C for 30 min. After centrifugation, cells were resuspended in PBS and filtered. Cell cycle analysis was then performed using flow cytometer.

4.12. Determination of caspase-3 in 8-treated HepG2 cells

In order to determine the **8** apoptotic potential, active caspase-3 level was measured in cell lysates using human caspase-3 ELISA kit obtained from Invitrogen (CA, USA), according to the manufacturer's instructions. Erlotinib was included in the assay as a reference.

4.13. In vitro enzyme inhibition assay against Hsp90

The most promising compound, **8**, was selected for *in vitro* enzyme inhibition screening assay against Hsp90 C-terminal domain using the Hsp90 (C-terminal) inhibitor screening assay kit (BPS Bioscience, USA), according to the manufacturer's instructions, in order to determine the IC_{50} of **8**. Briefly, wells of a microtiter plate were designated to substrate control, positive control, test inhibitor and blank. Aliquots of Hsp90 and its protein target (cyclophilin D), provided in the kit, were thawed on ice and diluted with assay buffers. Then, 4 µl of diluted Hsp α protein were added to each well designated for the positive control, test inhibitor and blank. To the wells designated for substrate control, 4 µl of Hsp90 assay buffer were added. Then, 2 µl of geldanamycin solution were added to wells designated for test inhibitor. For positive and substrate control wells, 2 µl of the same solution without inhibitor (inhibitor buffer) were added. Moreover, 4 µl of HspP90 assay buffer were added to blank wells. In order to initiate the reaction, cyclophilin D was diluted in assay buffer from which 4 µl were added to wells designated for substrate and positive controls as well as for test inhibitor. The plate was then incubated at room temperature for 30 min. Acceptor beads were added, then streptavidin-conjugated donor beads, followed by reading alpha-counts.

4.14. Determination of Hsp90 and Hsp90 client proteins in 8-treated HepG2 cells

The effect of **8** on Hsp90 and its client proteins; Akt, the hepatocyte growth factor (c-Met), c-Raf, and epidermal growth factor receptor (EGFR) was investigated using ELISA kits for human Hsp90 (Cloud-Clone Corp., USA), phospho-Akt (DRG International, USA), c-Met (Sigma Aldrich, USA), phospho-c-Raf (Cisbio, France), and EGFR (Raybiotech, USA), according to the manufacturers' instructions. For preparing cell lysates, cells were trypsinized and centrifuged following 72 h of treatment with **8**. The cell pellet was then washed with PBS and RIPA lysis buffer was used for cell lysis. Centrifugation was then performed to remove cell debris. Cell lysates were then collected and stored at −880 °C for performing the aforementioned ELISA assays.

4.15. Determination of Hsp70 in 8-treated HepG2 cells

To determine the effect of **8** on Hsp70, human Hsp70 ELISA kit (Cloud-Clone Corp., USA) was used according to the manufacturer's instructions. The assay was performed on cell lysates that were prepared, as explained earlier.

4.16. Statistical analysis

All values are presented as means ± standard deviation (S.D.) from three independent experiments performed in triplicates. Statistical analysis was performed by Student t test for unpaired data and One-Way Analysis of variance (ANOVA) followed by Bonferroni *post hoc* test for multiple comparisons using GraphPad Prism, version 5.0 (GraphPad Software, CA, USA) (v5). Statistical significance was determined at $P < 0.05$.

4.17. Molecular Modeling

4.17.1. Ligands preparation

The two **8** tautomers were constructed using Marvin Sketch 2D sketcher [30] and minimized using OpenBabel 2.4.1 [31] via Steepest Descent minimization algorithm for 100,000 steps and a convergence criterion of 10^{-6} kcal/mol/Å implementing MMFF94s (Merck Molecular Force Field static variant) [32] for stepwise energy calculations.

4.17.2. AutoDock vina docking

Receptors were fetched from PDB online database (http://www.rcsb.org/) [33]. Receptors and ligands were prepared using prepare_receptor4.py and prepare_ligands4.py scripts, respectively, implemented through AutoDock Tools 1.5.6 [34]. Protein and ligand preparations involved adding polar hydrogen atoms and Gasteiger partial charges. Single bonds of the ligands were considered rotatable while the binding site residues were considered rigid during the docking calculations. The search box was centered around the co-crystallized ligands and assigned 60 Å box side and 0.375 Å grid spacing. Box dimensions determination, writing AutoDock vina configuration files and docking automation were carried out using AutoDock/vina pymol plugin [35]. Docking calculations were carried out using AutoDock vina docking engine [29]. Crystallized water molecules were removed from protein before docking. AutoDock implements Lamarckian Genetic search Algorithm (LGA) where LGA runs were set to a value of 100 with 150 population size, 2,500,000 evaluations and 27,000 generations returning the best binding pose in the largest cluster. Binding energies are evaluated in terms of difference in Gibbs free energy (ΔG).

4.17.3. FRED Docking

Receptors were prepared using Make Receptor graphical utility and pdb2receptor utility program of OEDOCKING 3.2.0.2 of OpenEye Scientific Software [28]. Search box was determined around the co-crystallized ligands after cavity detection step using a molecular probe implemented through Make Receptor followed by a step of site shape potential detection. FRED docking engine requires a multiconformer ligand OpenEye binary file, so ligands were prepared using OpenEye OMEGA 3.0.1.2 conformer generation program [36]. FRED applies a systematic exhaustive search algorithm through rotational and translational degrees of freedom and evaluates the binding interactions using consensus Chemgauss4 scoring function.

All ligands and protein visualizations and figures generation were carried out using UCSF Chimera [26]. 2D interaction representation is generated by OpenEye toolkits [37].

4.17.4. Molecular Dynamics Simulations

The NAMD 2.12 package [38] was used for all the molecular dynamics simulation experiments. All system preparations were carried out using VMD 1.9.3 graphics software [39]. First, the protein molecule was stripped of any non-protein atoms (ligands, water and ions). Protein and ligand topology files were generated using VMD psfgen 1.6.4 package and SwissParam web server [40], respectively. The simulation systems were constructed manually by incorporating the topology files, solvating the protein-ligand complex in a box of TIP3P water solvent model with a 12 Å margin in all directions, using VMD solvate 1.7 package, and neutralizing the system charge with NaCl molecules, using VMD autoionize 1.4 package, ending up with systems of approximately 35,000 atoms. Periodic boundary conditions were considered during the simulations, wrapping all system atoms; by translating atoms that pass the periodic boundary to its mirror position on the opposite side of the cell.

100,000 minimization steps were carried out coupling the NAMD rigorous conjugate gradient algorithm with line search algorithm, followed by 10 ns NPT equilibration.

CHARMM36 Force Field [41] (July 2017 release) was used for providing protein parameters, whereas SwissParam parameter file was considered for ligands. The SwissParam derives the ligand atoms data from MMFF (Merck Molecular Force Field) [42], while Van de Waals parameters are taken from the closest atom type in CHARMM22 [41].

During dynamics calculations, any 1–2 and 1–3 atom interactions were neglected, and 1–4 interactions are fully considered. Van der Waals and electrostatic interactions are searched for in the system within a pair list distance of 13.5 Å, which is restarted once every integration cycle, and calculated with a 12 Å cut-off implementing function smoothing at 10 Å switch distance. For all runs, the velocity Verlet integration method was used for velocity and position

calculations with Particle Mesh Ewald Sum (PME) method for electrostatics calculations [43], and a 2 fs time step. 1 step size (2 fs) was set as frequency for non-bonded and full electrostatic interactions calculations. System temperature was kept constant at 310 K (37 °C) by controlling Kinetic Energy of the system using Langevin Dynamics with damping coefficient 1 ps^{-1} applying it to only heavy atoms. Pressure was also kept constant at 1 atm (1.01325 bar) using Langevin piston at 310 Kelvin with oscillation and damping periods of 200 and 50 fs, respectively, coupled with Nosé-Hoover method to control barostat fluctuations [44].

All dynamics simulations analysis was carried out using *ProDy* Python package [45] and VMD RMSD trajectory tool [39]. All analysis charts were constructed using Matplotlib 3.0.2 Python plotting library [46].

5. Conclusions

A series of 3,5-diarylpyrazoles has been synthesized and biologically evaluated against HepG2 and MCF7 cancer cell lines. Compound **8** exhibited cytotoxic potential against both cell lines yet a lower IC_{50} was reported on HepG2 cells. Hence, this compound was selected for further structure optimization and biological evaluation. Compound **8** caused cell cycle arrest at the G2 phase and showed apoptotic potential as evidenced by the increase in caspase-3 levels compared to control. Moreover, compound **8** exhibited potent inhibition of Hsp90 which was further validated by the degradation of the pro-survival client proteins (Akt, c-Met, c-Raf, and EGFR) and the increase in Hsp70 levels. Molecular docking and dynamics simulations were employed to predict the binding mode of **8**.

Declaration of Competing Interest

The authors have declared no conflict of interest.

Acknowledgements

This work was supported by The Center for Drug Research and Development (CDRD), Faculty of Pharmacy, The British University in Egypt, Grant 2019, and via a Natural Sciences and Engineering Research Council (NSERC) of Canada Discovery Grant (RGPIN-2017-04233) to SDT.

We gratefully acknowledge the support of OpenEye Scientific Software Inc. for offering an academic license.

We also gratefully acknowledge the support of NVIDIA Corporation with the donation of the Titan Xp GPU used for molecular dynamics calculations.

Appendix A. Supplementary material

Supplementary data to this article can be found online at https://doi.org/10.1016/j.bioorg.2019.103433.

References

[1] A. Forner, M. Reig, J. Bruix, Hepatocellular carcinoma, Lancet 391 (2018) 1301–1314.

[2] J.M. Llovet, S. Ricci, V. Mazzaferro, P. Hilgard, E. Gane, J.F. Blanc, A.C. de Oliveira, A. Santoro, J.L. Raoul, A. Forner, M. Schwartz, C. Porta, S. Zeuzem, L. Bolondi, T.F. Greten, P.R. Galle, J.F. Seitz, I. Borbath, D. Häussinger, T. Giannaris, M. Shan, M. Moscovici, D. Voliotis, J. Bruix, Sorafenib in advanced hepatocellular carcinoma, N. Engl. J. Med. 359 (2008) 378–390.

[3] L. Whitesell, S.L. Lindquist, Hsp90 and the chaperoning of cancer Nat, Rev. Cancer 5 (2005) 761–1722.

[4] (a) A. Maloney, P. Workmann, Hsp90 as a new therapeutic target for cancer therapy: the story unfolds, Expert Opin. Biol. Ther. 2 (2002) 3–24;
(b) R.E. Wang, Targeting heat shock proteins 70/90 and proteasome for cancer therapy, Curr. Med. Chem. 18 (2011) 4250–4264;
(c) F.U. Hartl, Molecular chaperones in cellular protein folding, Nature 381 (1996) 571–579.

[5] (a) For a complete list of Hsp90 interactoms see online comprehensive database of the Picard lab available at http://www.picard.ch/downloads/HSP90interactors.pdf. (b) See also, Advances in Cancer Research, Hsp90 in Cancer: Beyond the usual suspects. J. Isaacs, L. Whitesell 129 (2016), pp 1-20, Academic press.

[6] (a) I. Koca, A. Ozgur, M. Er, M. Gumus, K.A. Cosun, Y. Tutar, Design and synthesis of pyrimidinyl acyl thioureas as novel Hsp90 inhibitors in invasive ductal breast cancer and its bone metastasis, Eur. J. Med. Chem. 122 (2016) 280–290;
(b) C. Didelot, D. Lanneau, M. Brunet, A.L. Joly, A. De Theonel, G. Chiosis, C. Garrido, Anticancer therapeutic approaches based on intracellular and extracellular heat shock proteins, Curr. Med. Chem. 14 (2007) 2839–2847.

[7] (a) P. Workman, Combinatorial attack on multistep oncogenesis by inhibiting the Hsp90 molecular chaperone, Cancer Lett. 206 (2004) 149–157;
(b) J.R. Peter, C.C. Fritz, K.M. Depew, Discovery and development of Hsp90 inhibitors: a promising pathway for cancer therapy, Curr. Opin. Chem. Biol. 14 (2010) 412–420.

[8] A. Kamal, L. Thao, J. Sensintaffar, L. Zhang, M.F. Boehm, L.C. Fritz, F.J. Burrows, A high affinity conformation of Hsp90 confers tumour selectivity on Hsp90 inhibitors, Nature 425 (2003) 407–410.

[9] (a) C. Prodromou, The active life of Hsp90 complexes, Biochem. Biophys. Acta 2012 (1823) 614–623;
(b) A. Rohl, J. Rohrberg, J. Buchner, The chaperone Hsp90: changing partners for demanding clients, Trends Biochem. Sci. 38 (2013) 253–262.

[10] (a) T. Taldone, W. Sun, G. Chiosis, Discovery and development of heat shock protein 90 inhibitors, Biorg. Med. Chem. 17 (2009) 2225–2235;
(b) J. Trepel, M. Mollapur, G. Giaccone, L. Neckers, Targeting the dynamic Hsp90 complex in cancer, Nat. Rev. Cancer 10 (2010) 537–549;
(c) J.H. Jeong, Y.J. Oh, Y. Lho, S.Y. Park, K.H. Liu, E. Ha, Y.H. Seo, Targeting the entry region of Hsp90's ATP binding pocket with a novel 6,7-dihydrothieno [3,2-c] pyridine-5(4H)-yl amide, Eur. J. Med. Chem. 124 (2016) 1069–1080;
(d) A. Bargioti, L. Musso, S. Dallavalle, L. Merlini, G. Gallo, A. Ciacci, G. Giannini, W. Cabri, S. Penco, L. Vesci, M. Castorina, F.M. Milazzo, M.L. Cervoni, M. Barbarino, C. Pisano, C. Giommarelli, V. Zuco, M. De Cesare, F. Zunino, Isoxazolo-(aza)-naphthaquinones: a new class of cytotoxic Hsp90 inhibitors, Eur. J. Med. Chem. 53 (2012) 64–75;
(e) D. Chen, A. Shen, J. Li, F. Shi, W. Chen, J. Ren, H. Liu, Y. Xu, X. Wang, X. Yang, Y. Sun, M. Yang, J. He, Y. Wang, L. Zhang, M. Huang, M. Geng, B. Xiong, J. Shen, Discovery of potent N-(isoxazolyl-5-yl)amides as Hsp90 inhibitors, Eur. J. Med. Chem. 87 (2014) 765–781;
(f) D. Montoir, S. Barilli-Nion, A. Tonnerre, P. Juin, M. Duflos, M.A. Bazin, Novel 1,6-napthyridine-2(1H)-ones as potential anticancer agents targeting Hsp90, Eur. J. Med. Chem. 119 (2016) 17–33;
(g) F. Jiang, A.P. Guo, J.C. Xu, H.J. Wang, X.F. Mo, Q.D. You, X.L. Xu, Identification and optimization of novel 6-acylamino-2-aminoquinolines as potential Hsp90 C-terminal inhibitors, Eur. J. Med. Chem. 141 (2017) 1–14;
(h) C. Liang, X. Wu, Z. Li, J. Zhu, C. Lu, Y. Shen, Design, synthesis, and pharmacological evaluation of N-(5-chloro-2,4-dihydroxybenzoyl)-(R)-N-arylmethyl-1,2,3,4-tetrahydro-3-isoquinoline carboxamides as potent Hsp90 inhibitors, Eur. J. Med. Chem. 143 (2018) 85–96;
(i) S.Y. Park, Y.J. Oh, Y. Lho, J.H. Jeong, K.H. Liu, J. Song, S.H. Kim, E. Ha, Y.H. Seo, Design, synthesis, and biological evaluation of a series of resorcinol-based N-benzyl benzamide derivatives as potent Hsp90 inhibitors, Eur. J. Med. Chem. 143 (2018) 390–401;
(j) Q. Wei, J.Y. Ning, X. Dai, Y.D. Gao, L. Su, B.X. Zhao, Discovery of novel Hsp90 inhibitors that induced apoptosis and impaired autophagic flux in A549 lung cancer cells, Eur. J. Med. Chem. 145 (2018) 551–558;
(k) R. Ojha, H.L. Hung, W.C. Huangfu, Y.W. Wu, K. Nepali, M.J. Lai, C.J. Su, T.Y. Sung, Y.L. Chen, S.L. Pan, J.P. liou, 1-Aroylindoline-hydroxamic acids as anticancer agents, inhibitors of Hsp90 and HDAC, Eur. J. Med. Chem. 150 (2018) 667–677;
(l) X. Chen, P. Liu, Q. Wang, Y. Li, L. Fu, H. Fu, J. Zhu, Z. Chen, W. Zhu, C. Xie, L. lou, DCZ, 3112, a novel Hsp90 inhibitor, exerts potent antitumor activity against HER2-positive breast cancer through disruption of Hsp90-Cdc37 interaction, Cancer Lett. 434 (2018) 70–80;
(m) P.A. Brough, X. Barril, M. Beswick, B.W. Dymock, M.J. Drysdale, L. Wright, K. Grant, A. Massey, A. Surgenor, P. Workman, 3-(5-chloro-2,4-dihydroxyphenyl)-pyrazol-4-carboxamides as inhibitors of the Hsp90 molecular chaperone, Biorg. Med. Chem. Lett. 15 (2005) 5197–5201.

[11] K. Sidera, E. Patsavoudi, Hsp90 inhibitors: current development and potential in cancer therapy, Recent Pat. Anticancer Drug Discov. 9 (2014) 1–20.

[12] A. Ozgur, Y. Tutar, Heat shock protein 90 inhibitors in oncology, Curr. Proteomics 11 (2014) 2–16.

[13] L. Whitesell, E.G. Mimnaugh, B. De Costa, C.E. Myers, L.M. Neckers, Inhibition of heat shock protein Hsp90-pp60-src heteroprotein complex formation by benzoquinone ansamycins: essential role for stress proteins in oncogenic transformation, PNAS 91 (1994) 8324–8328.

[14] S.M. Roe, C. Prodromou, R. O' Brien, J.E. Ladburry, P.W. Piper, L.H. Pearl, Structural basis for inhibition of the Hsp90 molecular chaperone by the antitumor antibiotics radicicol and geldanamycin, J. Med. Chem. 42 (1999) 260–266.

[15] L. Neckers, P. Workman, Hsp90 molecular chaperone inhibitors: are we there yet? Clin. Cancer Res. 18 (2012) 64–76.

[16] S.R. Kasibhatla, K. Hong, M.A. Biamonte, D.J. Busch, P.L. Karjian, J.L. Sensintaffar, A. Kamal, R.E. Lough, J. Brekken, K. Lundgren, R. Grecko, G.A. Timony, Y. Ran, R. Mansfield, L.C. Fritz, E. Ulm, F.J. Burrows, M.F. Boehm, Rationally designed high-affinity 2-amino-6-halopurine heat shock protein 90 inhibitors that exhibit potent antitumor activity, J. Med. Chem. 50 (2007) 2767–2778.

[17] B.W. Dymock, X. Barril, P.A. Brough, J.E. Cansfield, A. Massey, E. McDonald,

R.E. Hubbard, A. Surgenor, S.D. Roughley, P. Webb, P. Workman, L. Wright, M.J. Drysdale, Novel, potent small-molecule inhibitors of the molecular chaperone Hsp90 discovered through structure-based design, J. Med. Chem. 48 (2005) 4212–4215.

[18] (a) P.A. Brough, W. Aherne, X. Barril, J. Borgognoni, K. Boxall, J.E. Cansfield, K.M.J. Cheung, I. Collins, N.G.M. Davies, M.J. Drysdale, B. Dymock, S.A. Eccles, H. Finch, A. Fink, A. Hayes, R. Howes, R.E. Hubbard, K. James, A.M. Jordan, A. Lockie, V. Martins, A. Massey, T.P. Mattews, E. McDonald, C.J. Northfield, L.H. Pearl, C. Prodromou, S. Ray, F.I. Raynaud, S.D. Roughley, S.Y. Sharp, A. Surgenor, D.L. Walmsey, P. Webb, M. Wood, P. Workman, L. Wright, 4,5-Diarylisoxazole Hsp90 chaperone inhibitors: potential therapeutic agents for the treatment of cancer, J. Med. Chem. 51 (2008) 196–218.

[19] K. Jhaveri, T. Taldone, S. Modi, G. Chiosis, Advances in the clinical development of heat shock protein 90 (Hsp90) inhibitors in cancers, Biochem. Biophys. Acta 2012 (1825) 742–755.

[20] S. Mohamady, B. Kralt, S.K. Samwel, S.D. Taylor, Efficient one-pot, two-component modular synthesis of 3,5-disubstituted pyrazoles, ACS Omega 3 (2018) 15566–15574.

[21] J.H. Jeong, Y.J. Oh, Y. Lho, S.Y. Park, K.H. Liu, E. Ha, Y.H. Seo, Targeting the entry region of Hsp90's ATP binding pocket with a novel 6,7-dihydrothieno[3,2-c]pyridin-5(4H)-yl amide, Eur. J. Med. Chem. 124 (2016) 1069–1080.

[22] R. Ojha, H.L. Huang, W.C. HuangFu, Y.W. Wu, K. Nepali, M.J. Lai, C.J. Su, T.Y. Sung, Y.L. Chen, S.L. Pan, J.P. Liou, 1-Aroylindoline-hydroxamic acids as anticancer agents, inhibitors of HSP90 and HDAC, Eur. J. Med. Chem. 150 (2018) 667–677.

[23] Y. Wang, Y.C. Koay, S.R. McAlpine, Redefining the phenotype of heat shock protein 90 (Hsp90) inhibitors, Chem. Eur. J. 23 (2017) 2010–2013.

[24] C.-C. Lee, T.-W. Lin, T.-P. Ko, A.H.-J. Wang, The hexameric structures of human heat shock protein 90, PLoS ONE 6 (2011) e19961.

[25] A. Šali, T.L. Blundell, Comparative protein modelling by satisfaction of spatial restraints, J. Mol. Biol. 234 (1993) 779–815.

[26] E.F. Pettersen, T.D. Goddard, C.C. Huang, G.S. Couch, D.M. Greenblatt, E.C. Meng, T.E. Ferrin, UCSF chimera – a visualization system for exploratory research and analysis, J. Comput. Chem. 25 (2004) 1605–1612.

[27] S. Terracciano, A. Russo, M.G. Chini, M.C. Vaccaro, M. Potenza, A. Vassallo, R. Riccio, G. Bifulco, I. Bruno, Discovery of new molecular entities able to strongly interfere with Hsp90 C-terminal domain, Sci. Rep. 8 (2018) 1709.

[28] (a) OEDOCKING 3.2.0.2: OpenEye scientific software, Santa Fe, NM. (http://www.eyesopen.com). (b) B.P. Kelley, S.P. Brown, G.L. Warren, S.W. Muchmore, POSIT: Flexible shape-guided docking for pose prediction. J. Chem. Inf. Model. 55 (2015) 1771-1780. (c) M. McGann, FRED Pose prediction and virtual screening accuracy, J. Chem. Inf. Model. 51 (2011) 578-596. (d) M. McGann, FRED and HYBRID docking performance on standardized datasets. J. Comput. Aided Mol. Des. 26 (2012) 897-906.

[29] O. Trott, A.J. Olson, AutoDockVina: improving the speed and accuracy of docking with a new scoring function, efficient optimization and multithreading, J. Comput. Chem. 31 (2010) 455–461.

[30] Marvin 18.10, 2018, ChemAxon, http://www.chemaxon.com.

[31] N.M. O'Boyle, M. Banck, C.A. James, C. Morley, T. Vandermeersch, G.R. Hutchison, OpenBabel: an open chemical toolbox, J. Cheminf. 3 (2011) 33–46.

[32] T.A. Halgren, MMFF VI. MMFF94s option for energy minimization studies, J. Comput. Chem. 20 (1998) 720–729.

[33] H.M. Berman, J. Westbrook, Z. Feng, G. Gilliland, T.N. Bhat, H. Weissig, I.N. Shindyalov, P.E. Bourne, The protein data bank, Nucl. Acids Res. 28 (2000) 235–242.

[34] (a) M.F. Sanner, Python: a programming language for software integration and development, J. Mol. Graphics Mod. 17 (1999) 57–61;
(b) G.M. Morris, R. Huey, W. Lindstrom, M.F. Sanner, R.K. Belew, D.S. Goodsell, A.J. Olson, Autodock4 and autodocktools4: automated docking with selective receptor flexiblity, J. Comput. Chem. 16 (2009) 2785–2791.

[35] D. Seeliger, B.L. de Groot, Ligand docking and binding site analysis with PyMOL and autodock/vina, J. Comput. Aided Mol. Des. 24 (2010) 417–422.

[36] OMEGA 3.0.1.2: OpenEye scientific software, Santa Fe, NM. (http://www.eyesopen.com). P.C.D. Hawkins, A.G. Skillman, G.L. Warren, B.A. Ellingson, M.T. Stahl, Conformer generation with OMEGA: algorithm and validation using high quality structures from the protein databank and the Cambridge structural database J. Chem. Inf. Model. 50 (2010) 572-584.

[37] OpenEye Toolkits 2017.Oct.1 OpenEye scientific software, Santa Fe, NM, http://www.eyesopen.com.

[38] J.C. Phillips, R. Braun, W. Wang, J. Gumbart, E. Tajkhorshid, E. Villa, C. Chipot, R.D. Skeel, L. Kale, K. Schulten, Scalable molecular dynamics with NAMD, J. Comput. Chem. 26 (2005) 1781–1802.

[39] W. Humphrey, A. Dalke, K. Schulten, VMD – visual molecular dynamics, J. Molec. Graphics 14 (1996) 33–38.

[40] V. Zoete, M.A. Cuendet, A. Grosdidier, O. Michielin, SwissParam, a fast force field generation tool for small organic molecules, J. Comput. Chem. 32 (2011) 2359–2368.

[41] (a) R.B. Best, X. Zhu, J. Shim, P.E.M. Lopes, J. Mittal, M. Feig, A.D. MacKerell Jr., Optimization of the additive CHARMM all-atom protein force field targeting improved sampling of the backbone phi, psi and side-chain chi1 and chi2 dihedral angles, J. Chem. Theory Comput. 8 (2012) 3257–3273;
(b) A.D. MacKerell Jr., M. Feig, C.L. Brooks III, Extending the treatment of backbone energetics in protein force fields: limitations of gas-phase quantum mechanics in reproducing protein conformational distributions in molecular dynamics simulations, J. Comput. Chem. 25 (2004) 1400–1415;
(c) A.D. MacKerell Jr., D. Bashford, M. Bellott, R.L. Dunbrack Jr., J.D. Evanseck, M.J. Field, S. Fischer, J. Gao, H. Guo, S. Ha, D. Joseph-McCarthy, L. Kuchnir, K. Kuczera, F.T.K. Lau, C. Mattos, S. Michnick, T. Ngo, D.T. Nguyen, B. Prodhom, W.E. Reiher III, B. Roux, M. Schlenkrich, J.C. Smith, R. Stote, J. Straub, M. Watanabe, J. Wiorkiewicz-Kuczera, D. Yin, M. Karplus, All-atom empirical potential for molecular modeling and dynamics studies of proteins, J. Phys. Chem. B 102 (1998) 3586–3616.

[42] T.A. Halgren, Merck molecular force field, I. J. Comput. Chem. 17 (1996) 490–519.

[43] U. Essmann, L. Perera, M.L. Berkowitz, T. Darden, H. Leem, L.G. Pedersen, A smooth particle mesh Ewald method, J. Chem. Phys. 103 (1995) 8577–8593.

[44] D.J. Evans, B.L. Holian, The nose-hoover thermostat, J. Chem. Phys. 83 (1985) 4069–4074.

[45] (a) A. Bakan, L.M. Meireles, I. Bahar, ProDy: protein dynamics inferred from theory and experiments, Bioinformatics 27 (2011) 1575–1577;
(b) A. Bakan, A. Dutta, W. Mao, Y. Liu, C. Chennubhotla, T.R. Lezon, I. Bahar, Evol and ProDy for bridging protein sequence evolution and structural dynamics, Bioinformatics 30 (2014) 2681–2683.

[46] J.D. Hunter, Matplotlib: a 2D graphics environment, Comput. Sci. Eng. 9 (2007) 90–95.